Supplementary Materials:

Materials and Methods

Figures S1-S20

References (49-70)

Materials and Methods:

BG505 SOSIP.664:PGV04, BG505 SOSIP.650:PGV04, and BG505 SOSIP.664 sample preparation for Electron Microscopy Analysis. Purified BG505 SOSIP.664 (*49*) at 0.25 mg/ml was incubated with a 10 fold molar excess of PGV04 Fab for 30 min. at 4°C. The mix was then loaded onto Superose 6 10/300 (GE Healthcare) and the fractions corresponding to the peak containing the BG505 SOSIP and PGV04 were concentrated using a centrifugal filter of 100-kDa cutoff (Millipore) to a final concentration of 0.72 mg/ml. Purified BG505 SOSIP.650 at 0.20 mg/ml was incubated with a 10 fold molar excess of PGV04 Fab for 30 min. at 4°C, and the complex was purified by size-exclusion chromatography and concentrated in a manner identical to BG505 SOSIP.664:PGV04. The final concentration before specimen vitrification was 1.5 mg/mL. For the unliganded trimer, BG505 SOSIP.664 at 0.20 mg/ml was further purified by size-exclusion chromatography and concentrated to a final concentration of 1.45 mg/mL before specimen vitrification. The final concentrations for the three different samples were selected empirically based on the observable number of particles after sample vitrification.

Specimen vitrification for cryo-electron microscopy. To avoid aggregation during vitrification, SOSIP specimens (BG505 SOSIP.664:PGV04, BG505 SOSIP.650:PGV04, and BG505

SOSIP.664) were incubated with a small amount of dodecyl maltoside (DDM); the final concentration of DDM was 0.085 mM (2x below the critical micelle concentration). All specimens were prepared for cryo-EM by applying 3 μL of sample to a freshly plasma cleaned holey carbon C-flat grid (Protochips, Inc.), allowing the sample to adsorb to the grid for 30 sec., followed by plunge-freezing into liquid ethane using a manual cryo-plunger in an ambient environment of 4°C.

Cryo-electron microscopy data collection and raw-frame alignment of BG505 SOSIP.664:PGV04. Data were acquired using the Leginon software (*50*) installed on a Tecnai F20 Twin transmission electron microscope operating at 200kV, with a dose of 32e^-/Å^2 and an estimated defocus ranging from 1.0-5.0 μm underfocus (distributed in an approximately Gaussian manner and centered at 2.9±0.8 μm). The dose was fractionated over 20 raw frames collected on the Gatan K2 Summit direct detection device, with each frame receiving a dose of ~8e^-/pixel/sec, as recommended and previously described (*51*). 6355 such "movies" were automatically collected and recorded at a nominal magnification of 29,000 x, corresponding to a pixel size of 1.21 Å at the specimen level. The individual frames were aligned using a GPU-enabled frame-alignment program that was generously provided by Yifan Cheng and Xueming Li. This program was used to track the global shifts between individual frames (*51*). Although we attempted to perform various dose-fractionation experiments with the final stacks, including removing the first frames, the last frames, and combinations thereof, the highest resolution and the best map was obtained using the full 32e^-/Å^2 dose.

Cryo-electron microscopy data collection of BG505 SOSIP.650:PGV04 and BG505 SOSIP.664 trimers. For both samples, data were acquired using the Leginon software (*50*) installed on a Tecnai F20 Twin transmission electron microscope operating at 200kV, with a dose of 32e^-/Å^2. The estimated defocus ranged from 1.0-4.5 μm underfocus for BG505 SOSIP.650:PGV04 (distributed in an approximately Gaussian manner and centered at 2.80±0.60 μm) and 1.0-5.0 μm for BG505 SOSIP.664 (distributed in an approximately Gaussian manner and centered at 2.95±1.00 μm). We acquired 945 images of BG505 SOSIP.650:PGV04 and 1112 images of BG505 SOSIP.664 on the TVIPS Tietz CMOS CCD 4Kx4K camera at a nominal magnification of 62,000x, corresponding to a pixel size of 1.36 Å at the specimen level.

Image processing and refinement of BG505 SOSIP.664:PGV04. Unless otherwise noted, all of the following image processing steps were performed within the Appion pipeline (*52, 53*). The CTF for all micrographs was estimated using the CTFFind3 package (*54*). All micrographs were also manually masked with the "manual masking" tool in Appion to remove regions that were over carbon and/or containing large amounts of disordered or aggregated particles. To obtain a clean stack of particles on which to perform the final refinement, we first performed an iterative stack cleaning procedure, described below. Particles were initially selected using Dog Picker (*55*) from 200 micrographs. A phase-flipped, contrast-inverted, and binned stack of 10k particles was created from these picks using a box size of 64 pixels and pixel size of 4.84 Å. The stack was subjected to reference-free 2D alignment and clustering using CL2D (*56*) to obtain 100 2D classes. The classes were inspected visually, and the best 12 were used as templates for template-based particle selection. Using these preliminary templates identified by reference-free 2D alignment and clustering, we selected particles over the entire set of micrographs using FindEM

(*57*) resulting in 475,234 selected particles from 6,488 micrographs. Micrographs were phase-flipped, contrast-inverted, and binned by 4, and subsequently individual particles were extracted using a box size of 64 pixels, corresponding to a pixel size of 4.84 Å. We performed 2D alignment and clustering using CL2D (*56*) to eliminate any particles that did not display identifiable features. Following the preliminary 2D alignment and clustering with CL2D, we performed another round of 2D alignment and clustering using ISAC (*58*), outside of Appion. The latter step eliminated particles that did not consistently produce stable reference free class averages. After manual micrograph masking, CL2D, and ISAC, 113,500 particles were retained for all subsequent analyses. The omitted particles likely suffered from drift, radiation damage, and/or poorly formed quaternary structure. An *ab initio* model was created from reference free 2D classes obtained from the raw particles using a customized approach for common-lines based 3D reconstructions (OptiMod, D.L., et al., manuscript submitted, fig. S12B). In addition, we also used a previously published low resolution cryo-electron tomographic reconstruction of viral surface trimeric gp160 (EMDB 5019) as an initial model (fig. S12C). Both initial models were used to independently refine the set of class averages. The refined maps resulting from either the *ab initio* common-lines approach or the previously published low-resolution tomographic reconstruction are essentially identical (fig. S12B-C). The two final maps were averaged together to provide the starting model for subsequent high-resolution analysis. To obtain initial Euler angles, an unbinned, phase-flipped, and contrast-inverted stack was generated from the original micrographs, corresponding to a box size of 256 pixels and pixel size of 1.21 Å. All subsequent steps were performed outside of Appion. Euler angles were assigned using the projection-matching protocol implemented within the Xmipp package (*59, 60*). After assigning the initial angles and shifts, the particle parameters were converted for use in Frealign (*61*). An

unbinned stack that had not been phase-flipped or contrast-inverted was used in the final parameter refinement in Frealign. During this step, we also performed a computational 3D sorting procedure to recover sub-stoichiometrically labeled SOSIP trimers, as described below.

3D sorting of BG505 SOSIP.664:PGV04. We used a map of BG505 SOSIP.664:PGV04 computed from the entire dataset as the starting point of 3D classification / sorting approach to determine which trimer particles were sub-stoichiometrically bound to Fabs. First, density corresponding to 1, 2, and all 3 Fabs was computationally subtracted from a binarized map of the 3-Fab-bound trimer. Subsequently, each of the four binarized maps, corresponding to gp140 with 3, 2, 1, and 0 Fabs bound, was applied as a mask to the 12 Å reconstruction, effectively removing a defined region. For each particle in the unsorted stack, Euler angles were assigned to each of the four volumes. Then, each particle was assigned to the stoichiometry group wherein the cross-correlation coefficient of the raw particle to the re-projection of each map along the assigned set of Euler angles was the highest. Using this approach, we generated 4 populations of particles – 49,572 particles corresponded to BG505 SOSIP.664 bound to 3 PGV04 Fabs (43.7% of the data); 40,817 particles corresponded to BG505 SOSIP.664 bound to 2 PGV04 Fabs (36.0% of the data); 17,972 particles corresponded to BG505 SOSIP.664 bound to 1 PGV04 Fab (15.3% of the data); 5,139 particles corresponded to BG505 SOSIP.664 without Fabs (4.5% of the data). From each population of particles, the previously assigned Euler angles enabled the reconstruction of an initial model for each of the four datasets. The sorted particles were then independently refined using each of the four reconstructed initial models and a resolution-limited approach in Frealign (*61*). For the 3-Fab and 2-Fab complexes, the resolution limit for Euler angle assignment was initially set to 25 Å for one iteration, then was dropped to 15 Å for the 2nd

iteration, and was further dropped to 10 Å for the 3rd and 4th iterations; for the 0-Fab and 1-Fab complexes, the resolution limit for Euler angle assignment never exceeded 25 Å. This conservative resolution-limited refinement ensured that the details recovered in each of the final maps did not result from noise bias and over-fitting, and that the sample is truly ordered beyond the resolution limit used to assign Euler angles (*62, 63*). Such a refinement scheme resulted in a resolution of 5.8 Å for SOSIP.664 with 3 Fabs (C3 symmetry and using 47,093 of the 49,572 particles [95%]), 7.9 Å for SOSIP.664 with 2 Fabs (C1 symmetry and using 38,776 of the 40,817 particles [95%]), 16.9 Å for SOSIP.664 with 1 Fab (C1 symmetry and using all 17,972 particles), and 19.1 Å for SOSIP.664 alone (C3 symmetry and using all 5,139 particles), all calculated using the 0.143 cutoff criterion in the Fourier Shell Correlation (FSC) curve (*64*). This overall classification and refinement scheme is summarized in fig. S11. We applied a negative temperature factor (*65*) of 550 to the final map containing 3 Fabs and 800 to the final map containing 2 Fabs. Lastly, to verify the quality of the computational separation of trimers exhibiting different Fab stoichiometries, reference-free 2D class averages were calculated from particles within each of the four stoichiometry groups, and Euler angles were assigned to the classes based on the final model computed from that stoichiometry group. Reference-free class averages and re-projections along the direction of the assigned Euler angles are displayed in figs. S12-S15. The close correspondence between the reference-free class averages and the re-projections of the 3D maps confirms that the vast majority of particles were correctly classified using the methods described above (figs. S12-S15).

Image processing and refinement of BG505 SOSIP.650:PGV04 trimers. Data were processed in a conceptually identical manner as for BG505 SOSIP.664:PGV04 described above, except for

specific differences that are indicated here. For all preliminary steps, BG505 SOSIP.650:PGV04 particles were binned by 4, which corresponded to a box size of 64 pixels and a pixel size of 5.46 Å. A stack of 10,614 particles remained after particle filtering using manual masking, CL2D, and ISAC, of which 10,083 contributed to the final reconstruction at 8.2 Å resolution (Fig 3E and fig. S8).

Image processing and refinement BG505 SOSIP.664 trimers. The unlabeled trimers derived from sorting the mixed dataset as described above results in a low resolution (19.1 Å) map. Thus, we collected and processed an independent dataset of trimers without the addition of PGV04 Fabs. Data were processed in a conceptually identical manner as for BG505 SOSIP.664:PGV04, described above, except for the specific differences indicated here. For all preliminary steps, BG505 SOSIP.664 particles were binned by 2, which corresponded to a box size of 80 pixels and a pixel size of 2.73 Å. A stack of 10,347 particles remained after particle filtering using manual masking and CL2D, of which 6,208 contributed to the final reconstruction at 12.7 Å resolution (fig. S6). We used a resolution-limited approach to Euler angle assignment (*60, 62*) implemented in Frealign; the low-resolution limit used to assign Euler angles was never decreased below 20 Å. Even by increasing the number of "particles" to beyond 100,000, we could never obtain a map of resolution higher than 12.7 Å. Notably, the quality of the HR1 helices also did not improve further with additional particles added. Thus, we believe that any nominal resolution gained by increasing the number of particles would be the product of over-fitting (*63, 64*), and 12.7 Å represents a current resolution limit for trimer-alone data, using our data acquisition and processing strategies and given the relatively small size and lack of features within BG505 SOSIP.664 in the absence of Fabs (figs. S6).

Comparison of PGV04-labeled and unlabeled protomers. Difference mapping between distinct protomers within the 2-Fab reconstruction (fig. S16) are described below. First, the 2-Fab volume was duplicated twice, and the duplicated volumes were rotated by 120° and 240°, respectively. All three volumes were then aligned to the 3-fold symmetrized reconstruction in Chimera (*66*), providing three distinct protomers in alignment with respect to each other. For a schematic, see fig. S16A. Differences were calculated using SPIDER (*67*) and are all displayed as positive differences at 2σ above the mean (fig. S16). Fig. S16 shows that, at this significance level, any differences that can be identified are minor and are predominantly scattered around the periphery of the protomer (fig. S16B). To identify regions where the differences are dominant, the difference densities were additionally low-pass filtered (fig. S16C). Since they are generated from less significant, scattered densities, such low-pass filtered representations cannot be interpreted as absolute differences; rather they describe the general extent and area within which minor differences are constrained.

Tilt-Pair analysis. Tilt-pair images were acquired with a tilt angle of 10° on a Tecnai F20 twin transmission electron microscope operating at 200 kV. Images were recorded at a nominal magnification of 50000x using a TVIPS Tietz F416 CMOS CCD camera, corresponding to a pixel size of 1.69 Å at the specimen level. An untilted and a tilted image were obtained of the same section of a grid, each with a dose of 16 e-/Å^2, for a combined dose of 32 e-/Å^2. This general strategy has been described previously (*65, 68*). 115 particle tilt-pairs were selected and binned by 2 to give a pixel size of 3.38 Å. Initial orientations were determined for both stacks using the 5.8 Å map of BG505 SOSIP.664 with 3 bound PGV04 Fabs and a projection-matching

routine in Xmipp. Subsequently, the orientations were refined with one cycle in Frealign. This strategy is analogous to all other refinements conducted in this study. A tilt-pair parameter plot (fig. S2B) was produced from the final parameters obtained for the tilted and untilted particles using the program Tiltdiff (*65, 68*).

High-resolution noise randomization to assess the degree of over-fitting. The high-resolution noise-randomization test (*69*) was applied to the BG505 SOSIP.664:PGV04 data to assess the degree of over-fitting within our refinement protocol. Phases within the 49,572 particle stack were randomized beyond 10 Å using the makestack_HRnoise.exe program that was generously provided by Richard Henderson. The phase-randomized stack was refined using an identical protocol as the non-phase-randomized data that is described above. Fourier shell correlation (FSC) curves between two half-maps reconstructed from the phase-randomized and non-phase randomized datasets were obtained using a spherical mask of either 210 Å of 100 Å diameter. The 210 Å diameter mask encompasses the entire structure with all three PGV04 Fabs; the 100 Å mask only encompasses the trimer core. The mask fall-off profile for both the 210 Å and 100 Å diameter masks was a cosine half-bell of width 20 pixels. FSC curves using the 210 Å diameter mask are displayed in fig. S2E and are intended to show the observable degree of over-fitting in the refinement protocol. FSC curves using the 100 Å mask that excludes large regions of noise between the trimer core and Fabs are displayed in fig. S2F and are intended to calculate the true resolution of the final reconstruction.

Model building and refinement. Various X-ray structures and fragments were used to fit into the EM maps, including gp120 bound to PGV04 (PDB 3SE9), V1/V2 (PDB 3U2S), gp120 core

plus V3 (PDB 2B4C), HR1 (PDB 1ENV) and HR2 (PDB 1ENV). Swiss model (*70*) was used to generate homology models of the x-ray structures with the BG505 sequence. These models were assembled into a composite model in PyMol (www.pymol.org) that was then relaxed into the EM map and energy minimized within Rosetta (*71*). A weight of 0.2 was applied for the EM map and 3-fold symmetry was enforced. Multiple refinements were done and produced structures that were within ~2 Å r.m.s.d. of each other. Glycans were placed into the EM density manually and not refined further.

CD4 binding sites models. X-ray structures of CD4bs antibodies in complex with gp120 monomers (PGV03: PDB 3SE8, PGV06: PDB 4JB9, 3BNC117: PDB 4JPV, 3BNC60: PDB 3RPI, CH103: PDB 3JAN, B12: PDB 2NY7, B13: PDB 3IDX, and F105: PDB 3HI1) were aligned to the gp120 region of the Env trimer in PyMol. Regions of the EM density map within 5 Å of the docked Fab/CD4 were colored yellow to indicate potential contacts. For b12, b13, and F105, the same procedure was followed, except regions within 2 Å were colored red to indicate potential clashes.

Figures. All figures were made using Chimera (*66*) and PyMol (www.pymol.org).

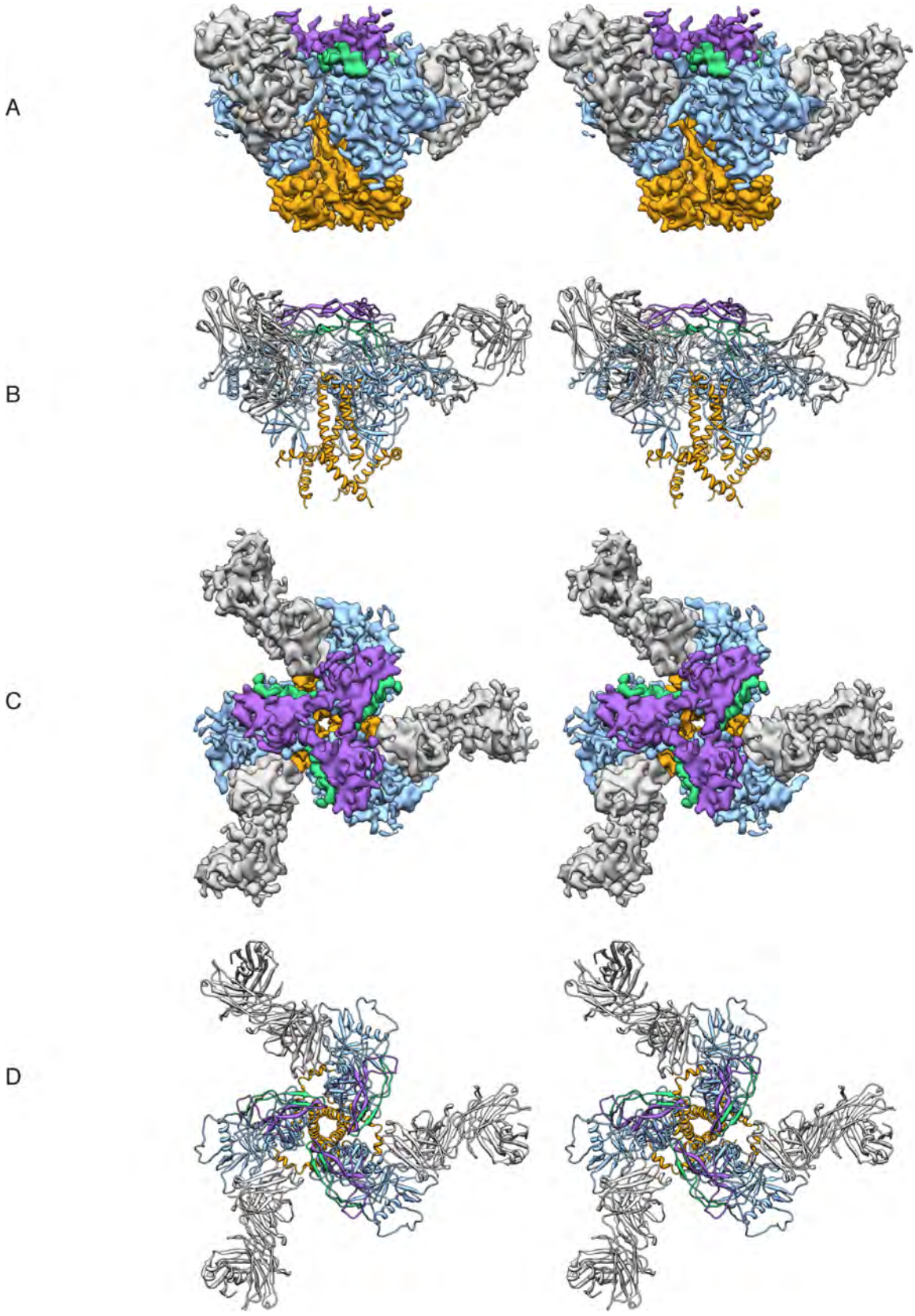
A
B
C
D

Fig. S1. Side and top views of the 5.8 Å EM reconstruction and corresponding model in stereo. **(A-B)** Side view of **(A)** EM map and **(B)** fitted model. **(C-D)** Top view of **(C)** EM map and **(D)** fitted model.

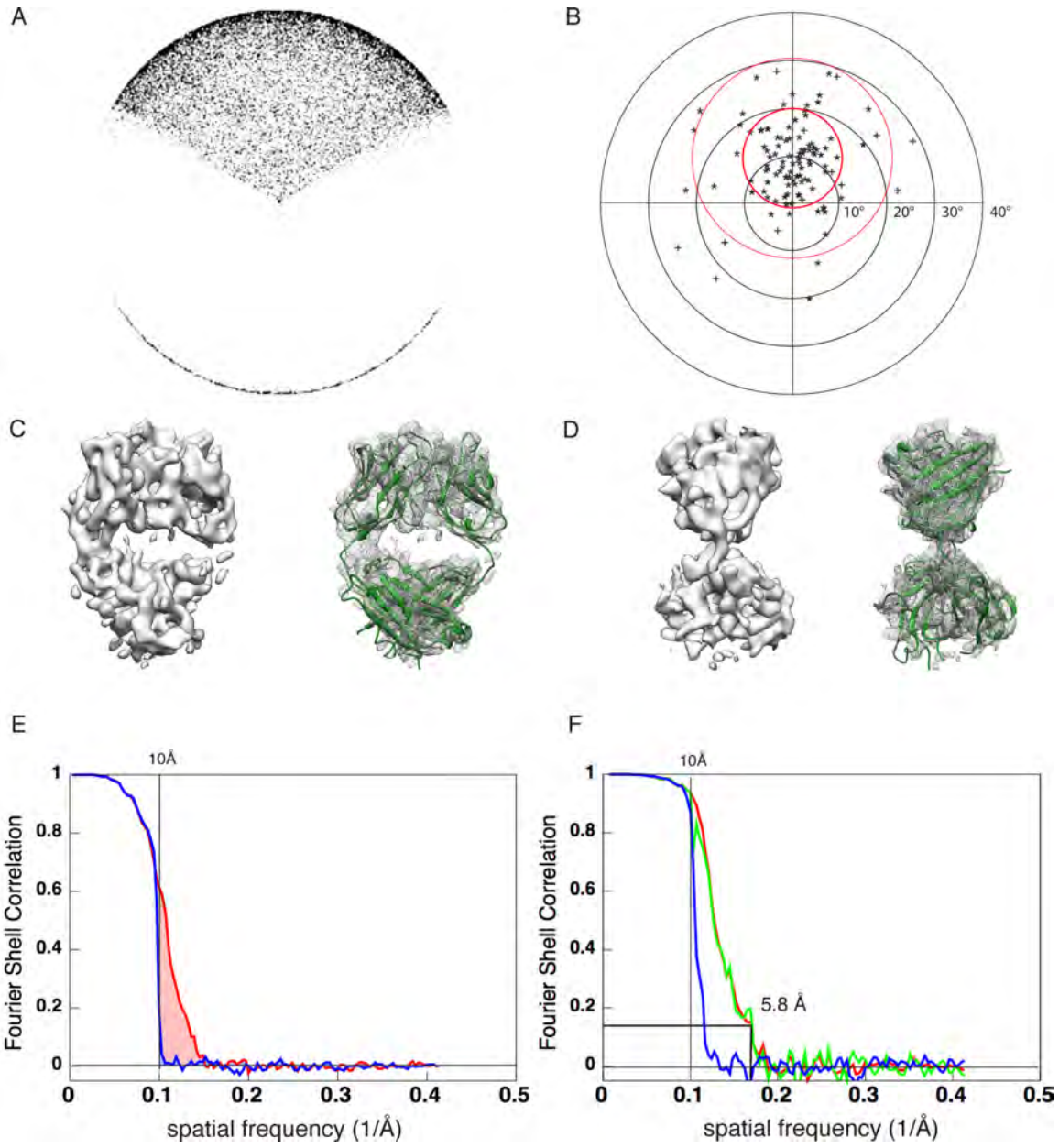

Fig. S2. Validation of the EM reconstruction. **(A)** Plot of Euler angle distribution for the final BG505 SOSIP.664:PGV04 reconstruction, showing an isotropic particle distribution. **(B)** Tilt-pair parameter plot (*68*) for the tilt-pair data of BG505 SOSIP.664:PGV04 particles. The nominal angle of the microscope stage used to collect the particle tilt-pairs was 10Å. The data points are centered at 9.9° with a standard deviation of 10.4°. Circular rings are shown on the plot to indicate 1 and 2 standard deviations of scatter about the mean value of 9.9°. **(C)** Top and

(D) side views of PGV04 Fab segmented from the EM map (left) and shown alongside the model from the crystal structure (PDB 3SE9) that is overlaid on the same segmentation (right). **(E-F)** Results of the high-resolution noise-randomization test (*69*) applied to the BG505 SOSIP.664:PGV04 refinement using two different spherical masks. **(E)** Result of the high-resolution noise-randomization test applied to the BG505 SOSIP.664:PGV04 refinement using a spherical 210 Å mask that encompasses the entire map. The Fourier shell correlation (FSC) curve is shown for the map described in this paper (red) and a map that was refined in an identical manner but using data where the high-resolution phases were randomized beyond 10 Å resolution (blue). Overfitting is shaded blue, while the difference between the two curves, which represents true features recovered from the data, is shaded light red. Using the resolution-limited refinement strategy described in the methods, we cannot observe any significant regions of overfitting. **(F)** Result of the high-resolution noise-randomization test applied to the BG505 SOSIP.664:PGV04 refinement using a spherical 100 Å mask that encompasses only the trimer core and intended to exclude solvent from the FSC calculation. The FSC curve is shown for the map described in this paper (red) and a map that was refined in an identical manner but using data where the high-resolution phases were randomized beyond 10 Å resolution (blue). The corrected, true FSC curve is displayed in green and reveals a nominal resolution value of 5.8 Å using the 0.143 cutoff criterion (*64, 65*).

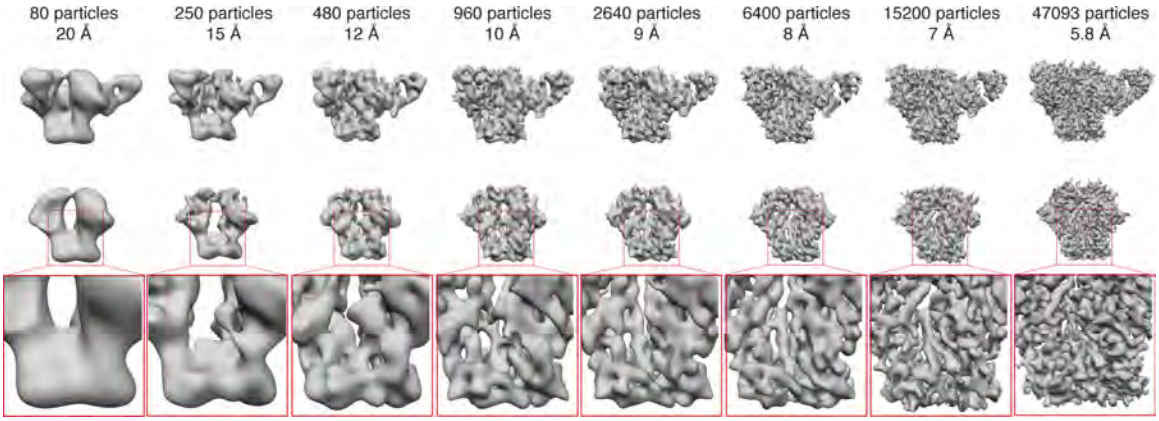

Fig. S3. Resolution-dependent features within EM reconstructions of the Env trimer. (A) Cryo-EM reconstructions of the trimeric SOSIP.664:PGV04 complex display features that are dependent upon the resolution of the electron potential map. Each column represents a distinct reconstruction, from 20 Å to 5.8 Å (left to right), using a portion of the complete 49,572-particle data set. The final resolution and the number of particles contributing to each map are specified for each reconstruction (note that only 47093 particles, or 95% of the stack, were used to obtain the final 5.8 Å map). Shown are: (top) the full SOSIP.664:PGV04 cryo-EM reconstruction, (middle) trimeric SOSIP.664, with PGV04 Fabs computationally removed, and (bottom) a close-up view of the boxed region above. At and below 15 Å resolution, a hole is observed within trimeric SOSIP.664, similar to what has been previously reported using tomographic methods (EMDB 5458). At higher resolutions, this hole is less evident. At ~12 Å resolution, the central HR helices begin to appear and by ~9 Å resolution, the helices become recognizably cylindrical. At ~7 Å resolution, gp120 loops are apparent. This suggests that the previously identified hole in the Env trimer is an artifact that is only observed in lower resolution reconstructions. At the final 5.8 Å resolution, features can be identified at approximately equally spaced increments that likely correspond to a combination of the α-helical pitch and bulky side chains. These features are particularly apparent within helices HR1 and HR2.

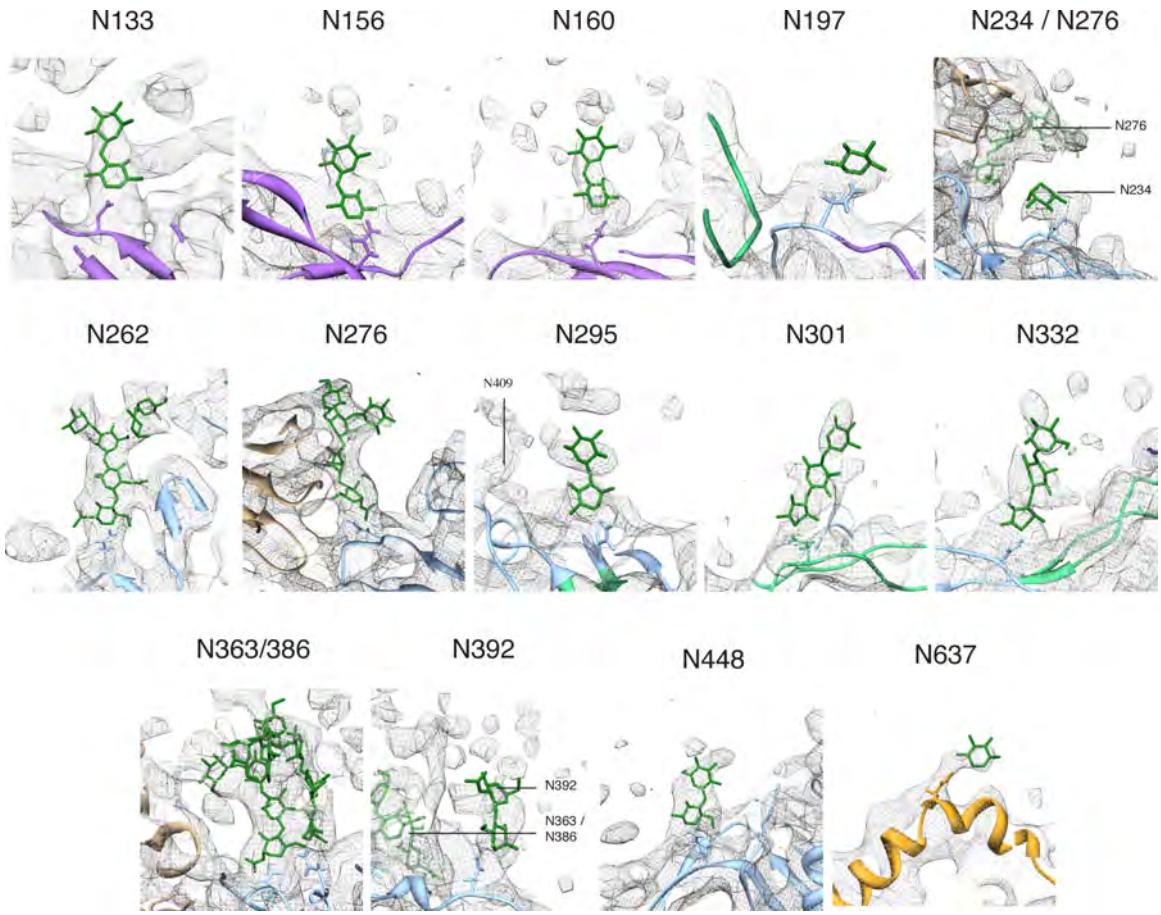

Fig. S4. Density corresponding to predicted glycan positions. Glycans are positioned into the EM density when continuous density can be seen emanating from the underlying peptide. Density features that are discontinuous most likely correspond to the branched chain of the specified glycans, but are not explicitly defined due to uncertainly in their position. In some cases, it was not possible to discriminate between two glycans that are in close proximity (e.g. N363/N386 and, to a lesser extent, N392). In these cases, multiple glycans are docked.

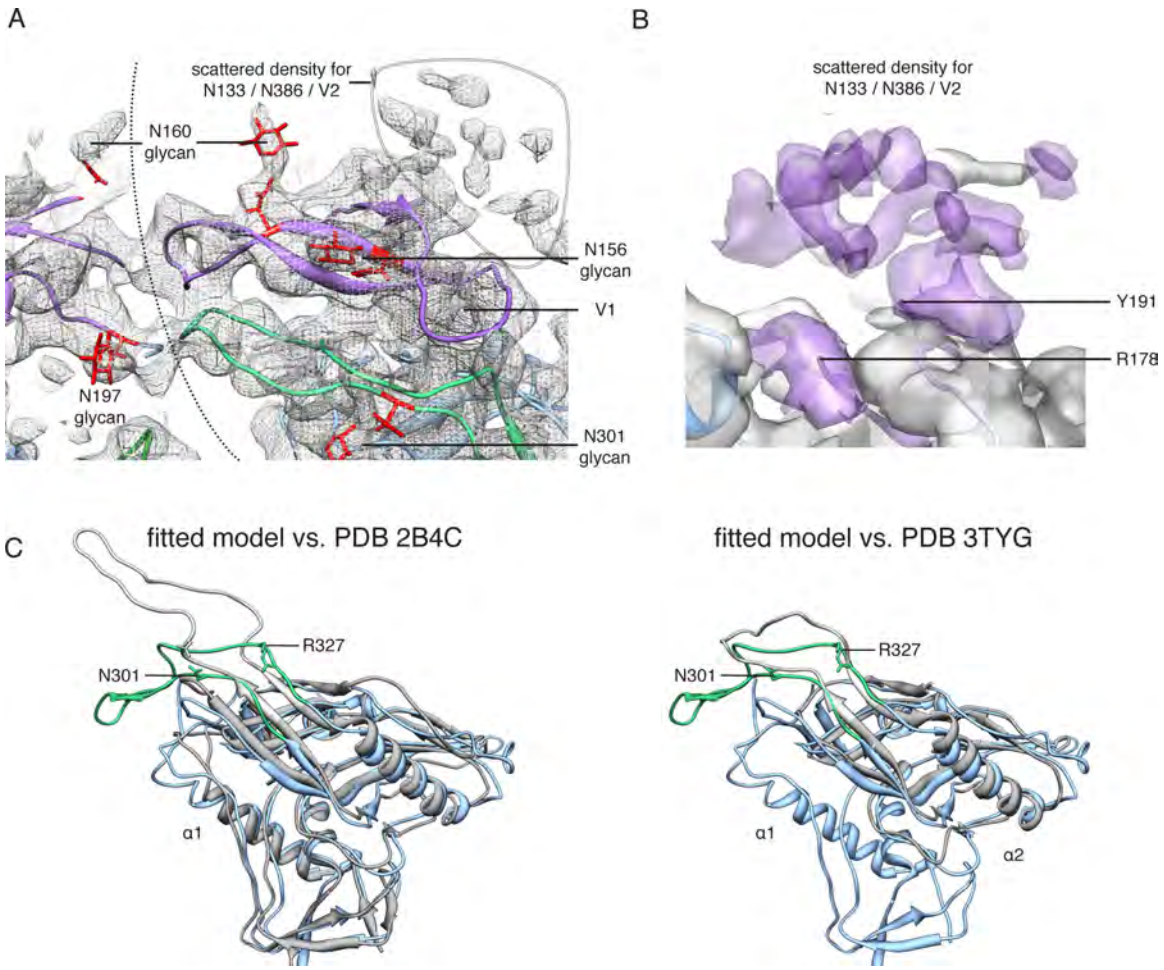

Fig. S5. Supplemental data for core gp120 and variable loops (A) EM density with the fitted model for regions of V1/V2 and V3. The interface with the adjacent protomer is shown by a curved dotted line. Putative density for V2 and nearby glycans is circled at top right. **(B)** Density shot of V2 and nearby glycans. The region between R178 and Y191 could not be modeled. **(C)** Comparison of the V3 loop from the EM model (blue) with the X-ray structures of the full-length (PDB 2B4C) and mini-V3 (PDB 3TYG). Residues 1-90 and 126-196 are omitted for clarity.

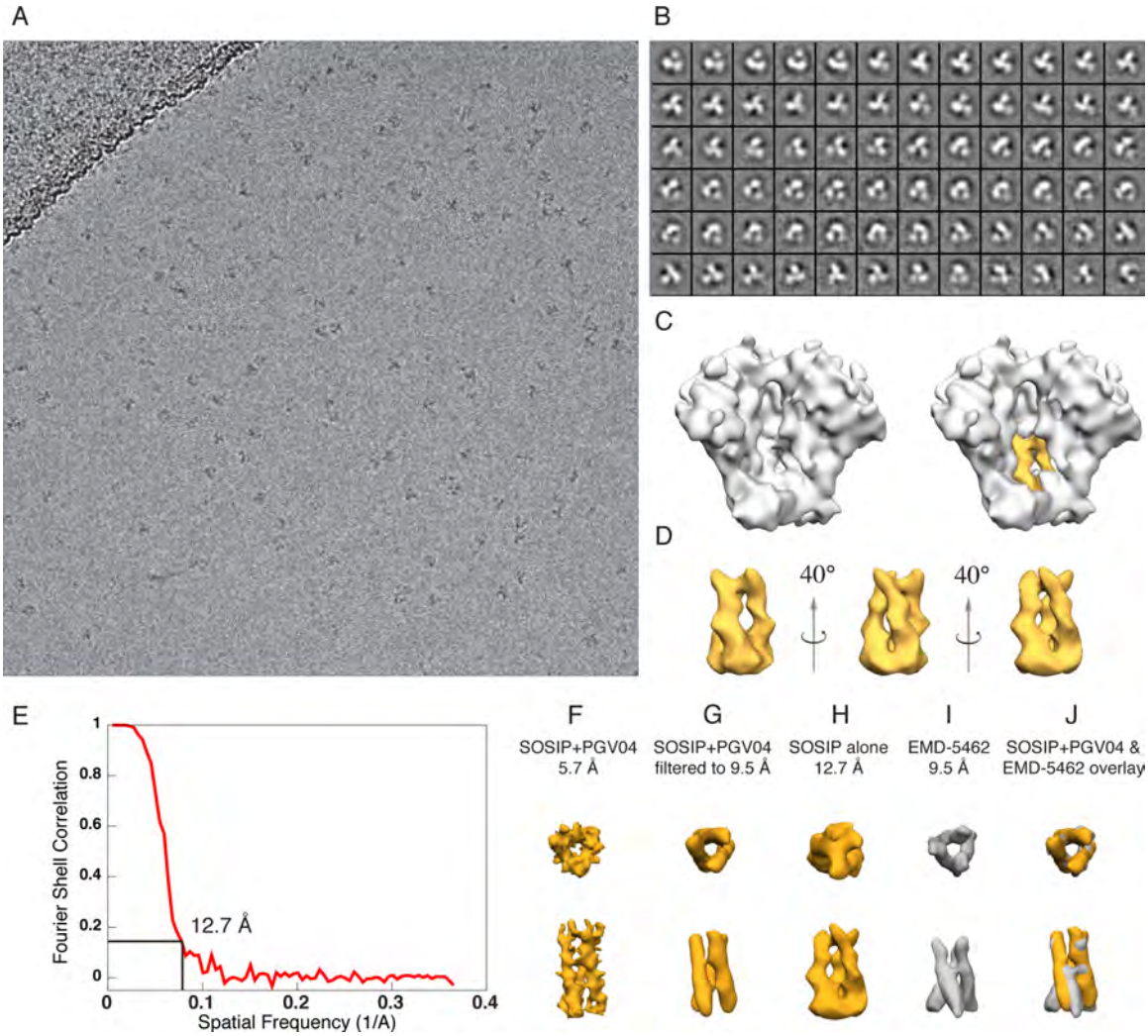

Fig. S6. Image processing of BG505 SOSIP.664 in the absence of Fabs. (**A**) Micrograph of a frozen hydrated preparation of BG505 SOSIP.664, imaged at 3.5 μm underfocus. (**B**) Reference-free class averages from the data. (**C**) Refined map from 6,208 particles. (**D**) As C, but with the three internal HR1 helices segmented and displayed in yellow. (**E**) Resolution curve showing an estimated value of 12.7 Å using the 0.143 cutoff criterion. We were not able to reconstruct a higher resolution map of the unliganded trimer due to lack of features and mass, and the limits of our current imaging and processing capabilities. (**F-J**) Comparison of the pre-fusion 3-helix bundle between different reconstructions. Displayed are helices from **(F)** BG505

SOSIP.664:PGV04 reconstruction at 5.8 Å resolution described here, **(G)** as **F**, but filtered to 9.5 Å resolution, **(H)** SOSIP.664 alone in the absence of Fabs, **(I)** KNH SOSIP.681 from (EMD-5462), and **(J)** and overlay of **G** and **I**.

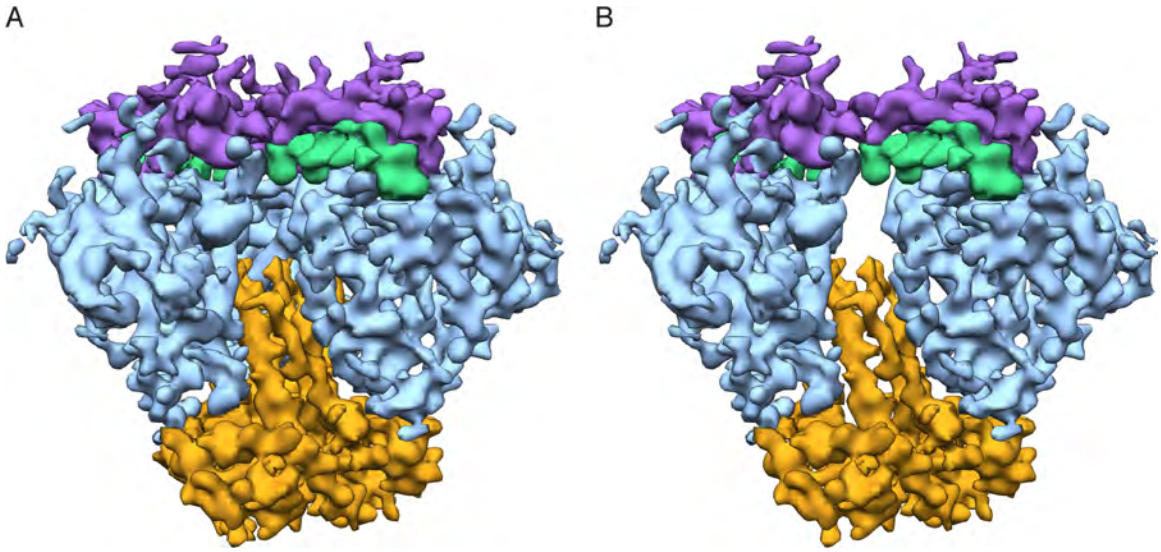

Fig. S7. Small opening evident within the trimer core. Side view of the segmented trimer EM map shown with the back protomer in place (A), and removed (B) to accentuate the opening. This opening is also present in the same relative position in influenza hemagglutinin (see Fig. 3 in (*49*))

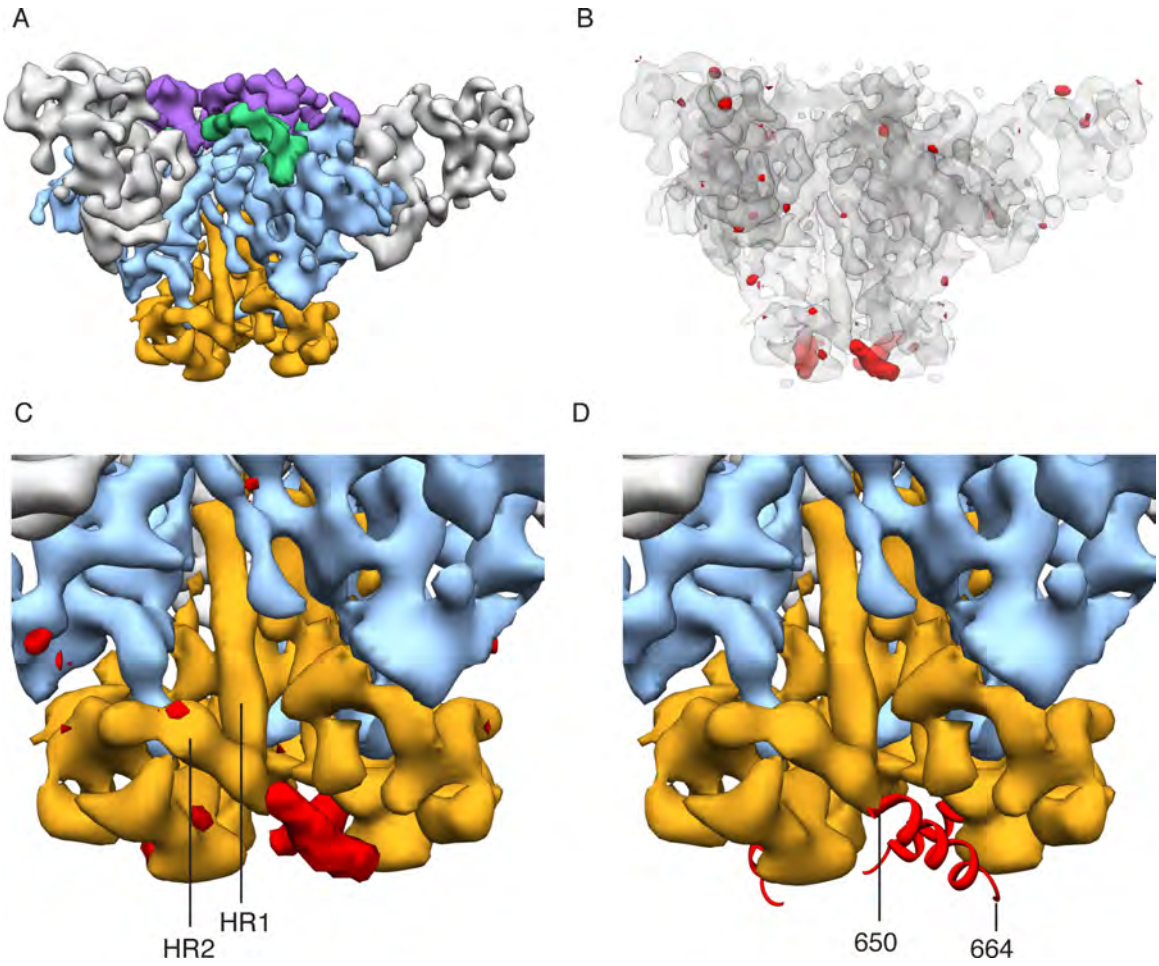

Fig. S8. Difference data for BG505 SOSIP.650:PGV04 (A) Segmented SOSIP.650:PGV04 reconstruction. (B) Difference map between SOSIP.664:PGV04 and SOSIP.650:PGV04 (red) overlaid on the SOSIP.650:PGV04 reconstruction (gray). Difference density is shown at two standard deviations above the mean pixel value. **(C-D)** Zoomed in image showing the gp41 base with **(C)** the difference density from **B** (red) and **(D)** the modeled region of gp41 described in this study. Missing density in **C** corresponds to an approximately 14 amino-acid truncation from the C-terminal residue 664.

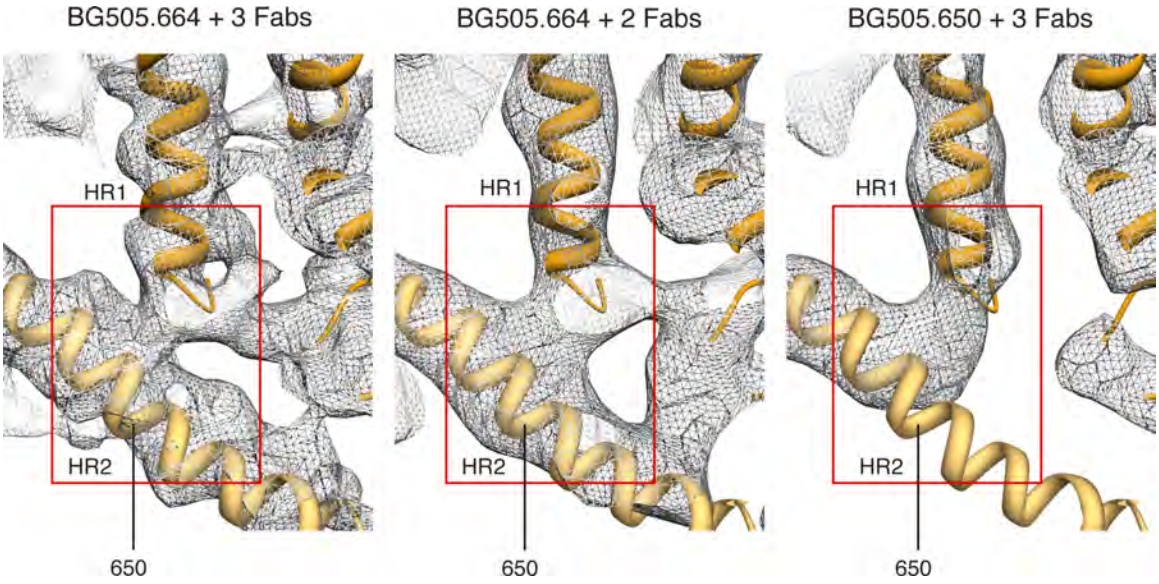

Fig. S9. Interaction between HR1 and HR2 in gp41. Strong connectivity is observed between the base of HR1 and the area surrounding residues 647-650 within HR2 in three independently observed EM maps.

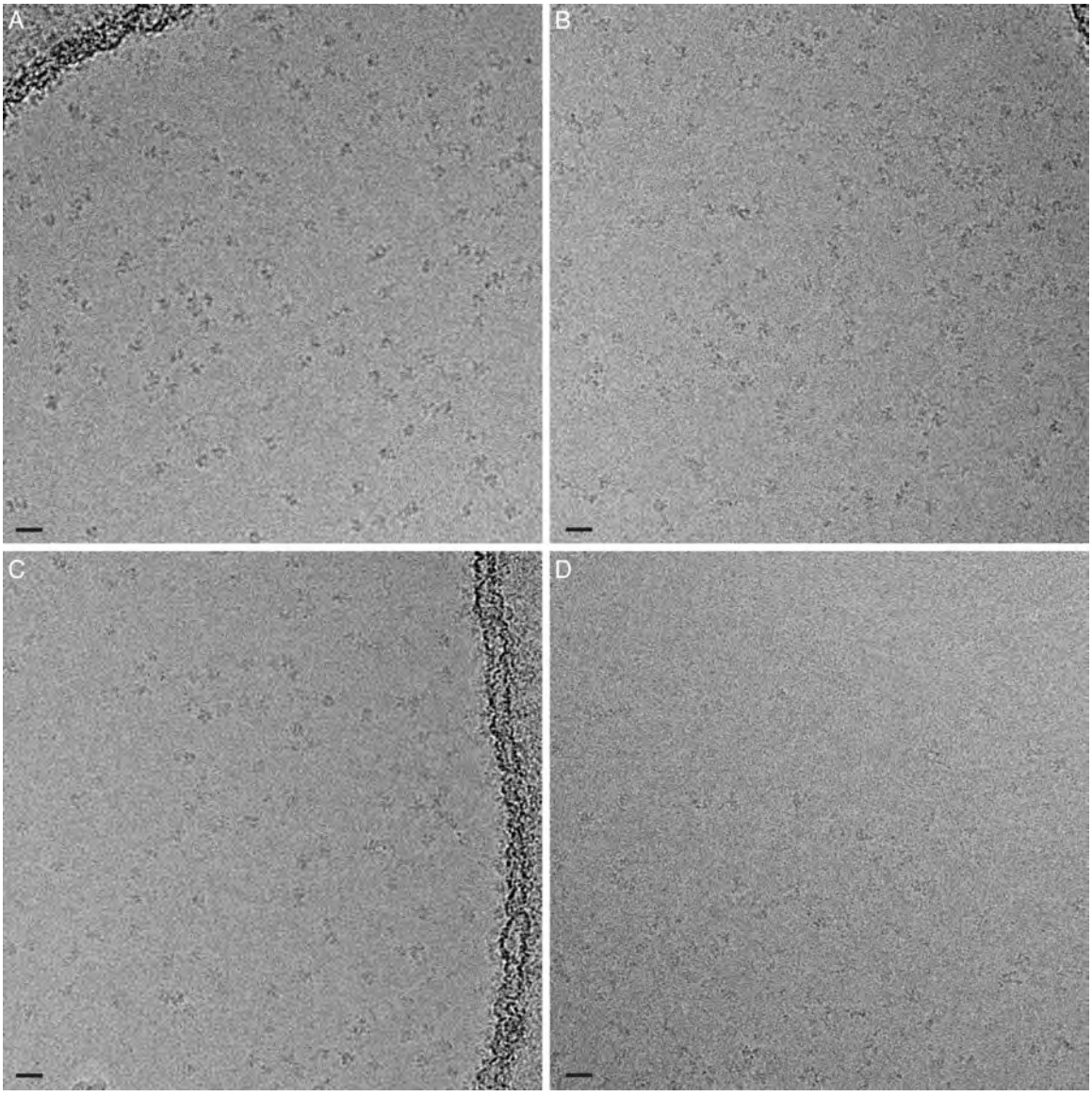

Fig. S10. Micrographs of BG505 SOSIP.664 trimers bound to PGV04. Electron micrographs are shown at **(A)** 4.5 μm, **(B)** 3.5 μm, **(C)** 3.0 μm, and **(D)** 2.0 μm underfocus. Below 2 μm underfocus, the particles were difficult to identify visually.

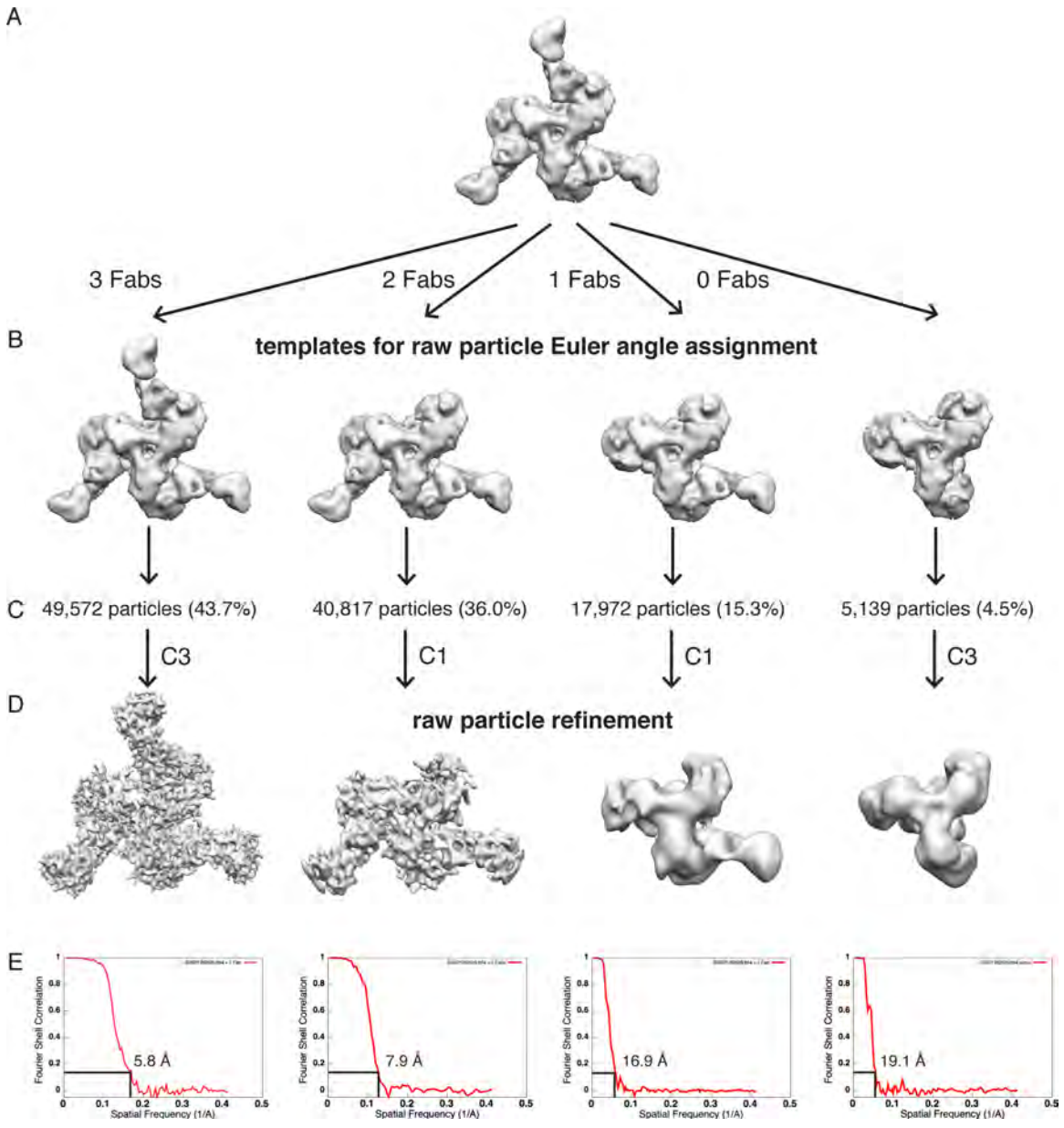

Fig. S11. **Sorting scheme for reference-based classification**. **(A)** A single-model refinement of BG505 SOSIP.664 trimers bound to PGV04 served as a starting model. **(B)** Fabs were computationally removed to produce 4 distinct references (templates) for 3D classification, labeled "3 Fabs", "2 Fabs", "1 Fab" and "0 Fabs", respectively. **(C)** The 3D templates were used to sort all the unprocessed particles. 3D Euler angle assignment and correlation-based classification resulted in four different particle populations. **(D)** The four particle populations

were independently refined using a reconstructed model from the assigned Euler angles as a reference to produce final maps. **(E)** FSC curves from the individual refinements of the four distinct particle populations. The values are based on the 0.143 cutoff criterion – 5.8 Å for the 3 Fab reconstruction, 7.9 Å for the 2 Fab reconstruction, 16.9 Å for the 1 Fab reconstruction, and 19.1 Å for the 0 Fab reconstruction.

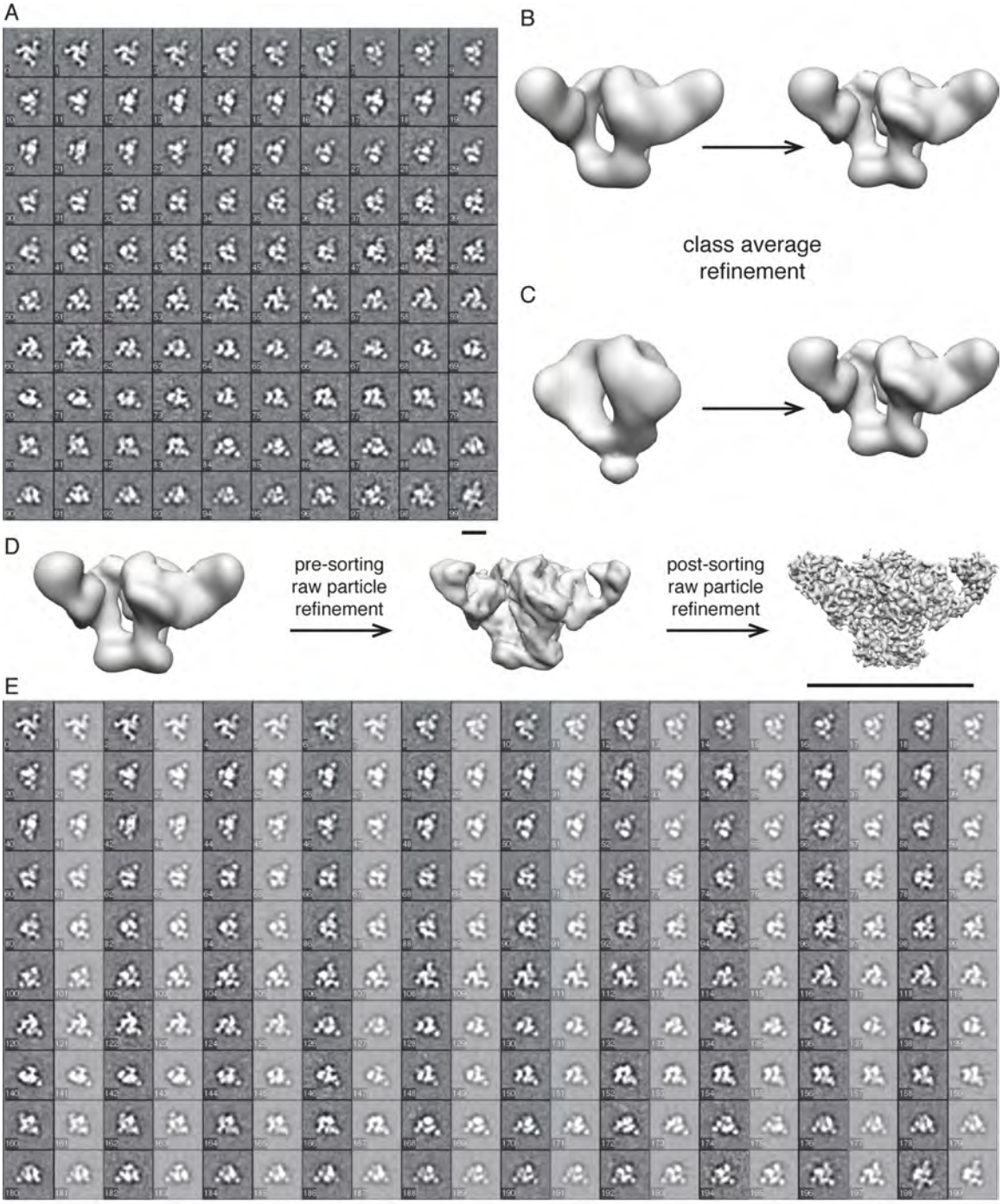

Fig. S12. Image processing of BG505 SOSIP.664 with 3 PGV04 Fabs. **(A)** reference-free 2D class averages obtained using ISAC (*58*). **(B)** Refinement of the 2D class averages using an *ab initio* model calculated using OptiMod (D.L., et al., manuscript submitted). **(C)** Refinement of the 2D class averages using EMD-5019 as a starting model. **(D)** Progression of the refinement:

(left) the refined map from **C**; (center) density map before particle sorting and without sharpening; (right) final density map. **(E)** Comparison of the reference-free class averages from **A** (unshaded) with re-projections of the 3-Fab model from **C** along identical Euler angles (lightly shaded).

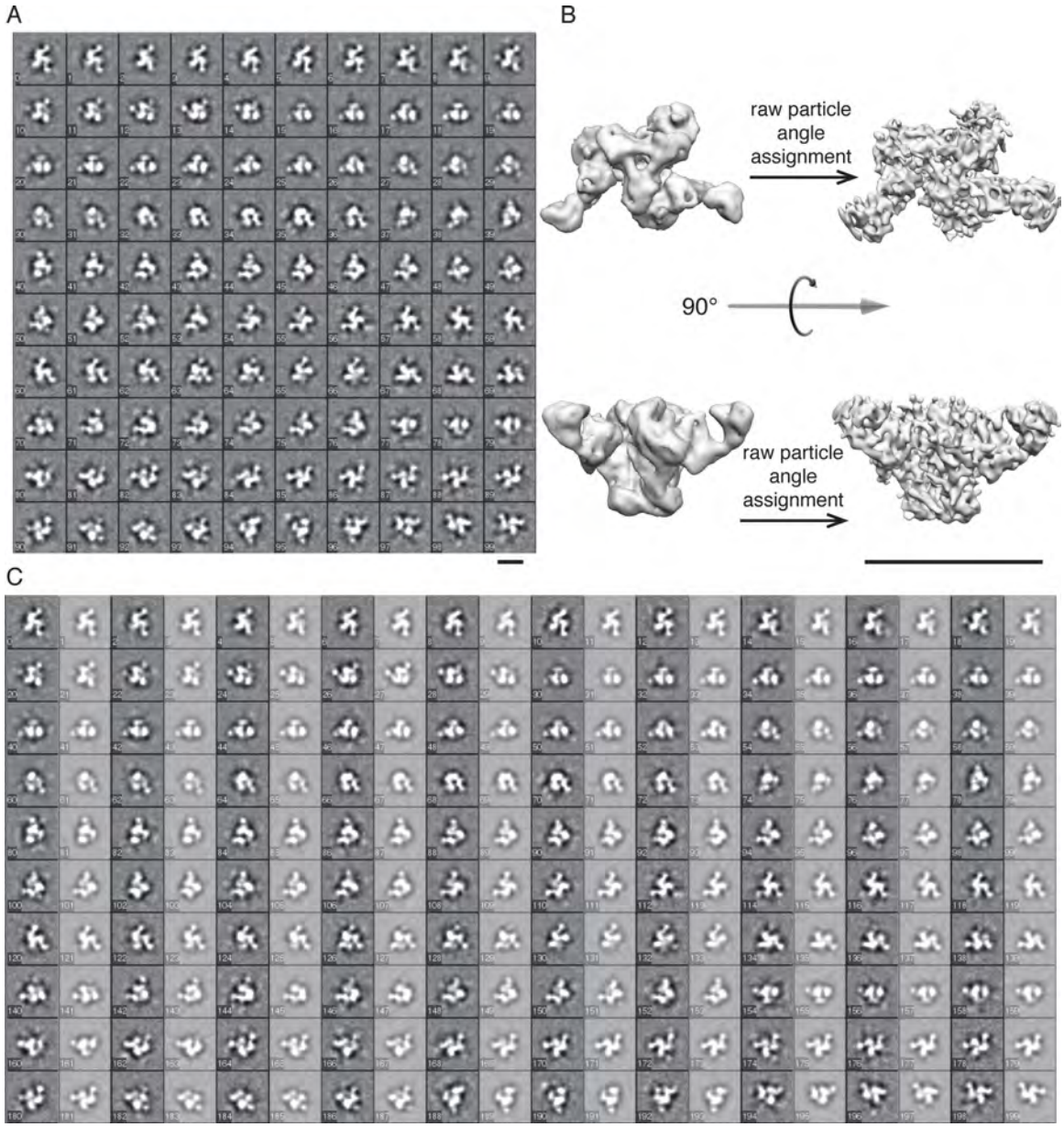

Fig. S13. Image processing of BG505 SOSIP.664 with 2 PGV04 Fabs. **(A)** reference-free 2D class averages obtained using ISAC (*58*). **(B)** Top (top) and side (bottom) views showing (left) the starting model before 3D sorting (left) and (right) the final model after 3D sorting and raw particle refinement. **(C)** Comparison of the reference-free class averages from **A** (unshaded) with re-projections of the final 2-Fab reconstruction from **B** along identical Euler angles (lightly shaded).

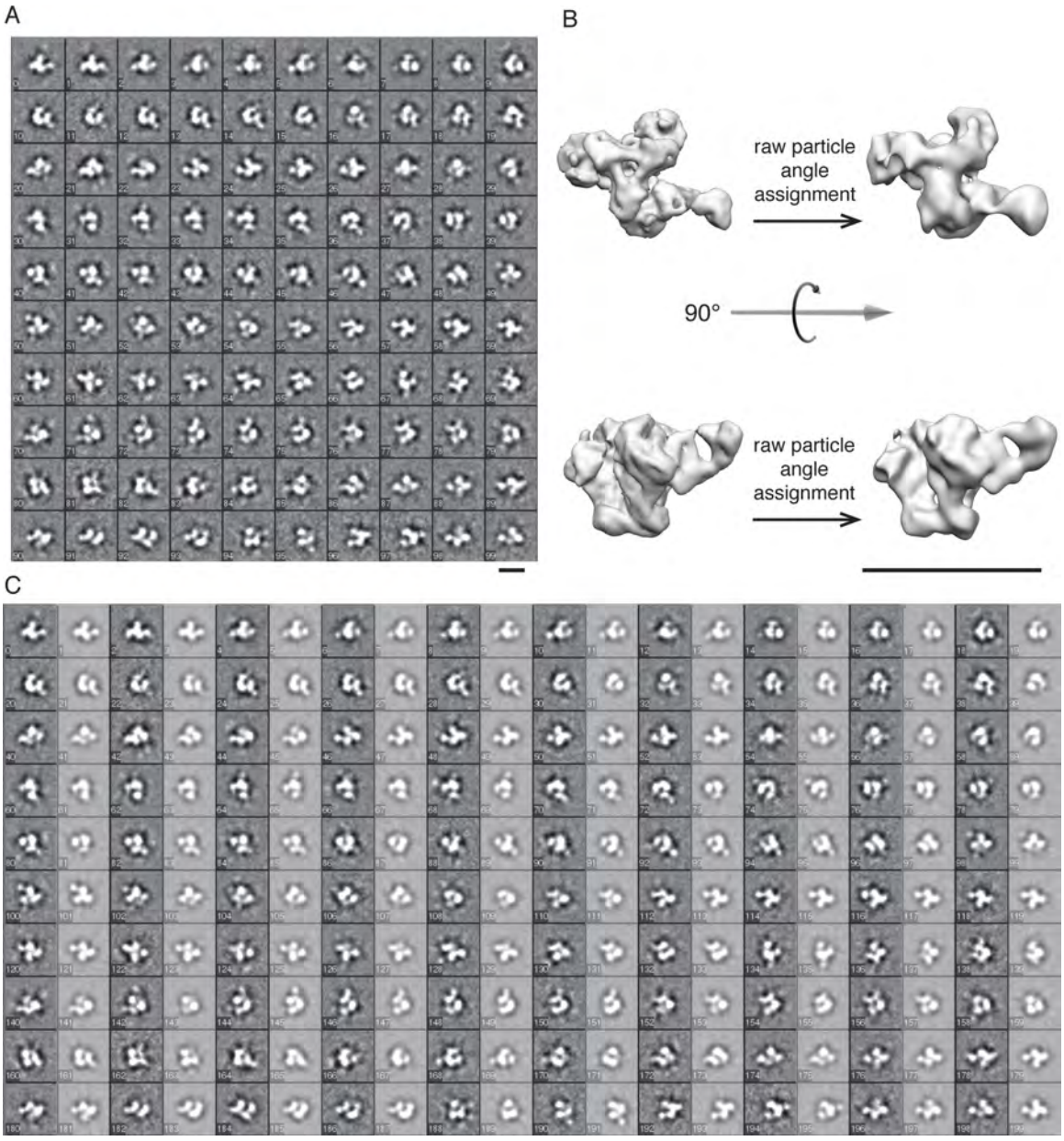

Fig. S14. Image processing of BG505 SOSIP.664 with 1 PGV04 Fabs. (A) reference-free 2D class averages obtained using ISAC (*58*). **(B)** Top (top) and side (bottom) views showing (left) the starting model before 3D sorting and (right) the final model after 3D sorting and raw particle refinement. **(C)** Comparison of the reference-free class averages from **A** (unshaded) with re-projections of the final 1-Fab reconstruction from **B** along identical Euler angles (lightly shaded).

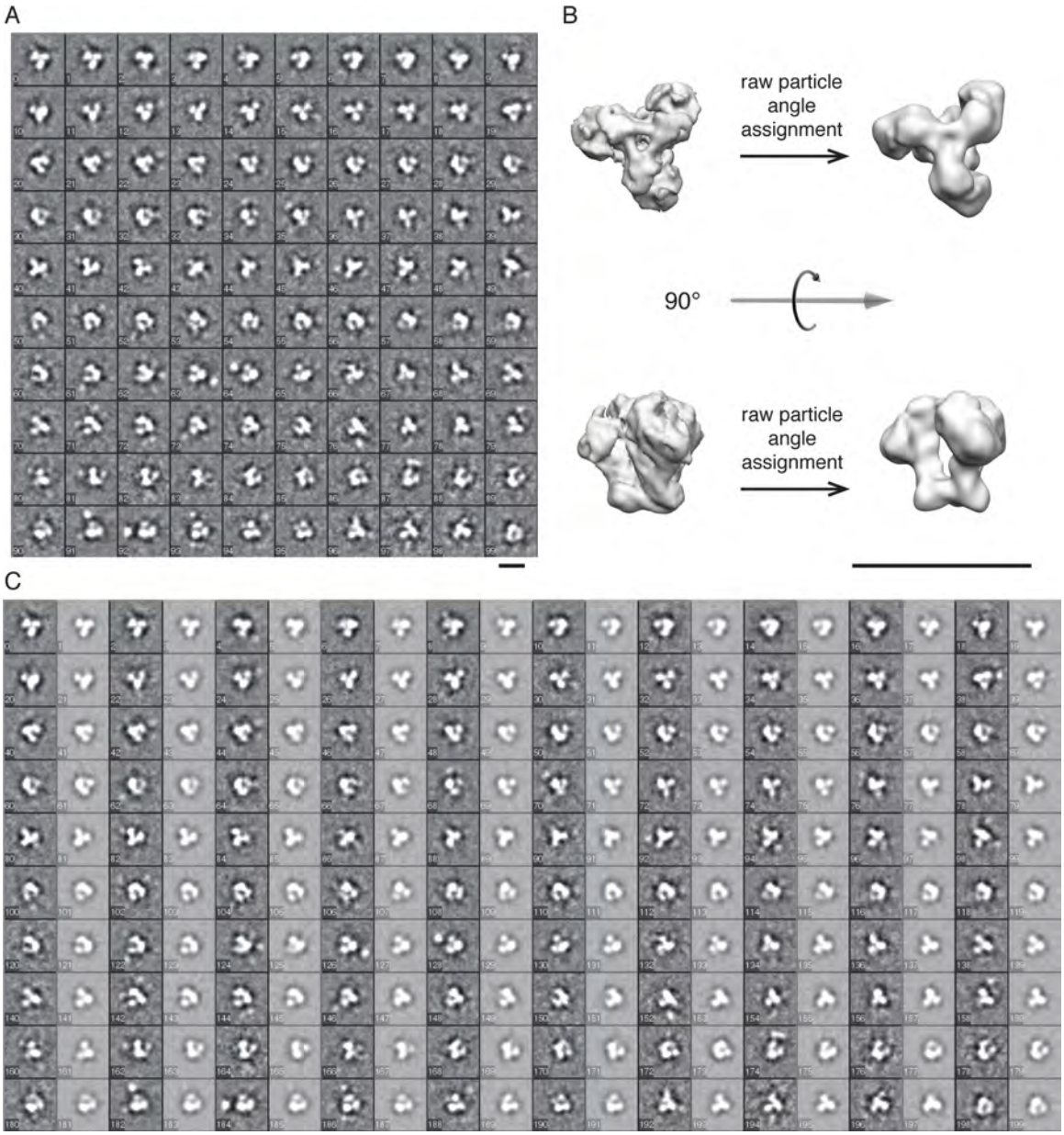

Fig. S15. Image processing of BG505 SOSIP.664 without PGV04 Fabs. **(A)** reference-free 2D class averages obtained using ISAC (*58*). **(B)** Top (top) and side (bottom) views showing (left) the starting model before 3D sorting and (right) the final model after 3D sorting and raw particle refinement. **(C)** Comparison of the reference-free class averages from **A** (unshaded) with re-projections of the final 0-Fab recontruction from **B** along identical Euler angles (lightly shaded).

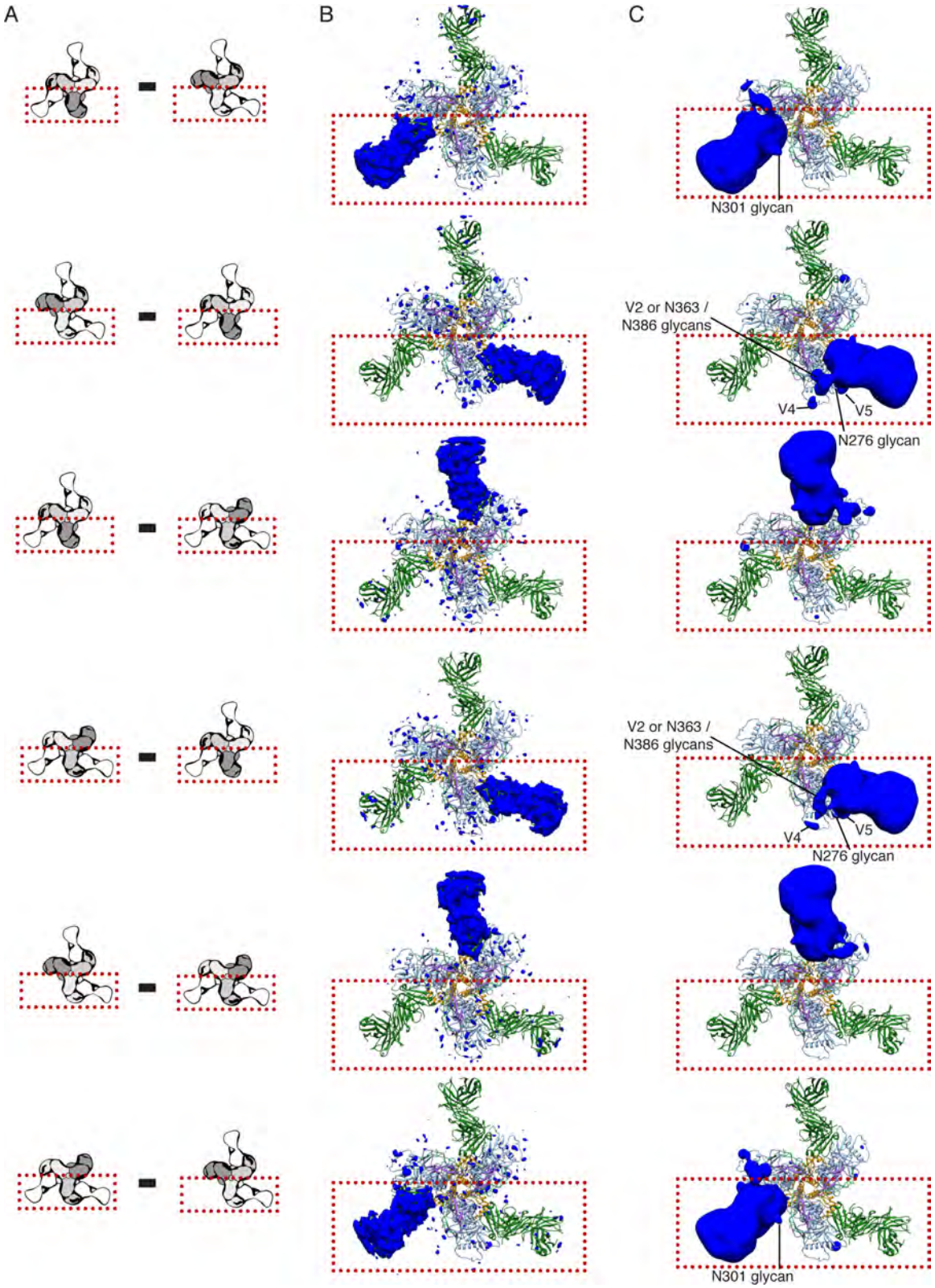
A
B
C
N301 glycan
V2 or N363 /
N386 glycans
V4
V5
N276 glycan
V2 or N363 /
N386 glycans
V4
V5
N276 glycan
N301 glycan

Fig. S16. Difference maps calculated between all combinations of protomers within the 2-Fab BG505 SOSIP.664:PGV04 reconstruction. **(A)** Schematic illustrating the difference calculations performed between distinct protomers. Each of the three protomers is shaded dark, medium, and light gray. **(B)** Raw difference maps between all combinations of protomers displayed at 2 standard deviations above the mean. With the exception of the missing Fab, only minor changes are observed. **(C)** Filtered difference maps indicating that the presence of Fab increases local ordering of multiple indicated regions adjacent to (e.g. N363/386 glycans/V2 loop, V5 loop, and N276) and across from (e.g. N301 glycan) the CD4 binding site. In all panels **A-C**, the region of interest is outlined with a dotted red rectangle.

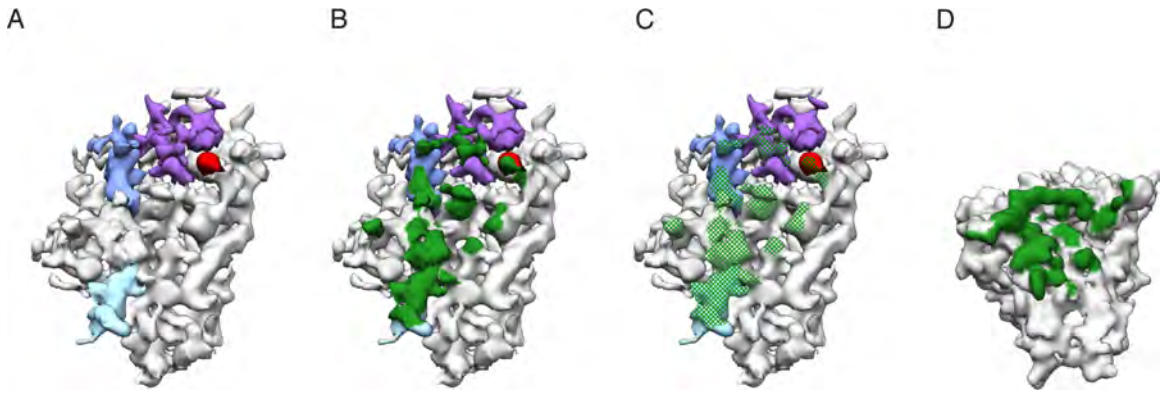

Fig S17. Elaborated nature of the CD4 binding site. (A) Segmentation of the elaborated gp120 subunit from the EM map. Densities of interest are highlighted (N197 is colored red; N276 is colored light blue; N363/N386 are colored blue; V2 and/or portions of neighboring protruding glycans are colored purple). **(B-C)** The full PGV04 epitope on the trimer within 5 Å of the PGV04 Fab is denoted by **(B)** a solid green and **(C)** green cross-hatching. The expanded epitope shows that densities corresponding to glycans and V2 are positioned to influence how the CD4bs is recognized. A glycan at N276 makes extensive interactions with the light chain of PGV04. **(D)** The PGV04 epitope from the crystal structure in complex with the gp120 core monomer (PDB 3SE9) is shown. The area displayed within 5 Å of PGV04 is colored green on the surface view of core monomeric gp120 that has been filtered to 5.8 Å.

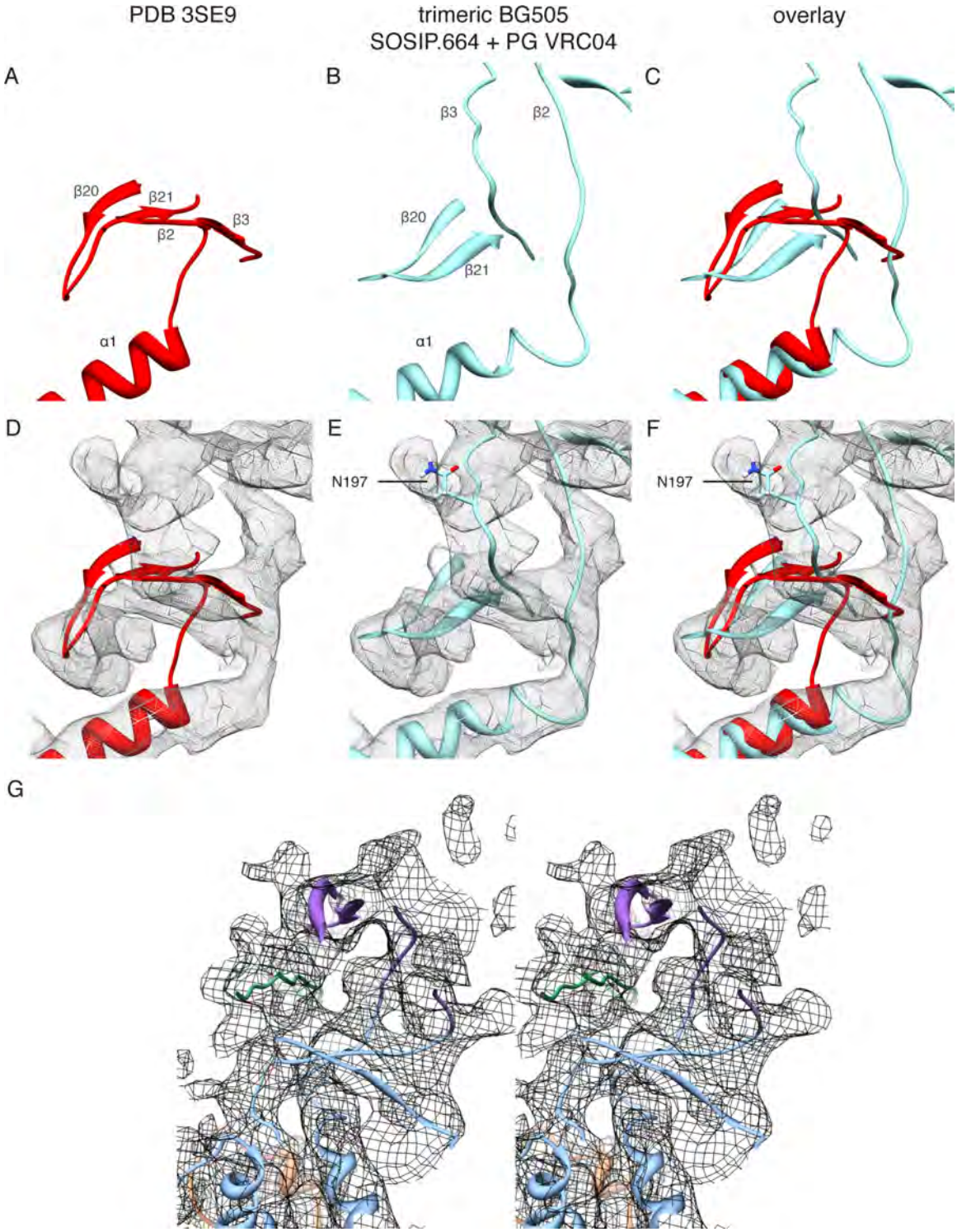

Fig. S18. Comparison of bridging sheet between monomeric and trimeric gp120. The bridging sheet area accounts for a portion of the CD4 binding site within gp120. **(A)** A ribbon

model of the bridging sheet from core gp120 bound to PGV04 (PDB 3SE9) is shown along **(B)** the same region in the fitted model of BG505 SOSIP.664:PGV04 from this study. **(C)** Overlay of the models from **A-B**. **(D-F)** Same as **(A-C)** but overlaid on the EM density. Regions of interest are indicated throughout the panels. **(G)** Stereo view of gp120, including V1/V2 (V1/V2 – purple; gp12 – blue; V3 – green).

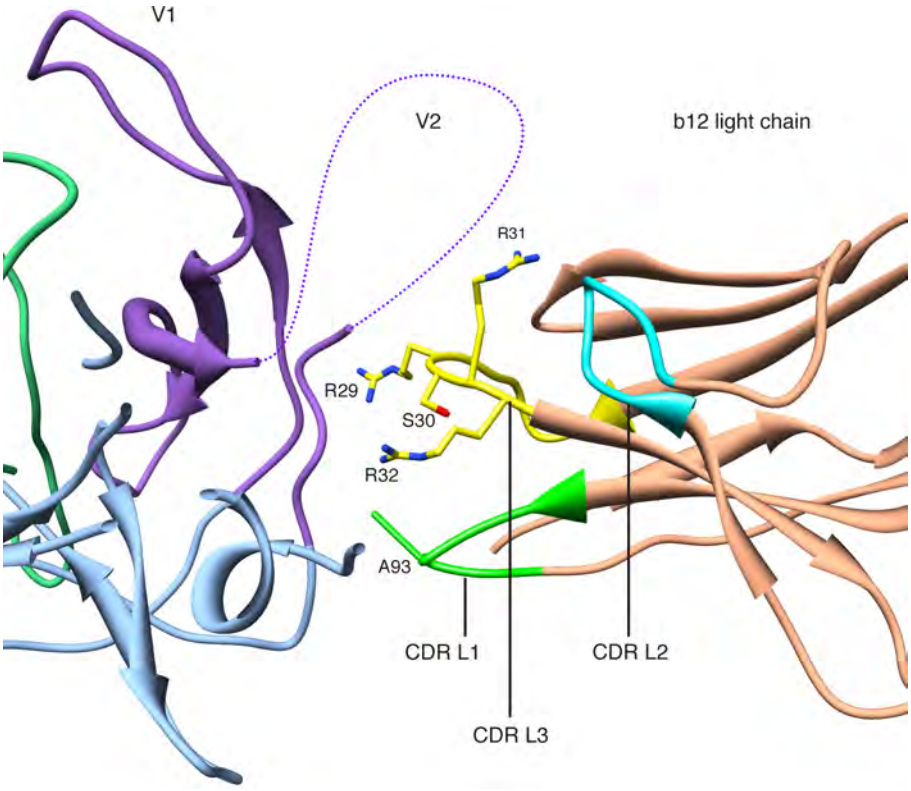

Fig. S19. Model of b12 light chain interaction with V1/V2. Close up view of the docked b12 Fab structure (PDB 2NY7) into the trimer. The residues indicated are positioned to interact with V1/V2 in the trimer (V1/V2 – purple; gp12 – blue; V3 – green; b12 – beige; CDR L1 – light green; CDR L2 – cyan; CDR L3 yellow).

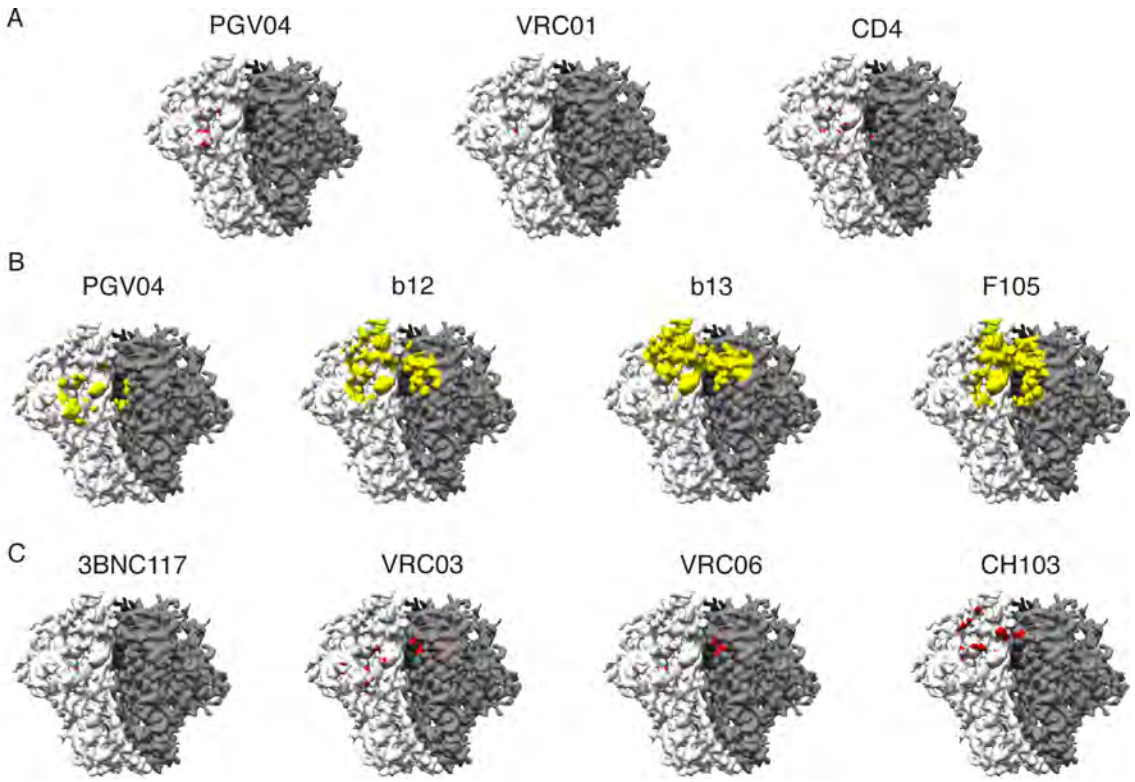

Fig. S20. Quaternary nature of CD4 binding site. **(A)** All regions of the EM map within 2 Å of PGV04, VRC01, and CD4 have been colored red. **(B)** All regions of the EM map within 5 Å of PGV04, b12, b13, and F105 have been colored yellow. **(C)** All regions of the EM map within 2 Å of 3BNC117, VRC03, VRC06, and CH103 have been colored red.

References:

49. J. P. Julien *et al.*, Crystal structure of a soluble cleaved HIV-1 Env trimer in complex with a glycan-dependent broadly neutralizing antibody. *Science*, (2013).

50. C. Suloway *et al.*, Automated molecular microscopy: the new Leginon system. *Journal of structural biology* **151**, 41 (Jul, 2005).

51. X. Li *et al.*, Electron counting and beam-induced motion correction enable near-atomic-resolution single-particle cryo-EM. *Nature methods* **10**, 584 (Jun, 2013).

52. D. Lyumkis *et al.*, Automation in single-particle electron microscopy connecting the pieces. *Methods in enzymology* **483**, 291 (2010).

53. G. C. Lander *et al.*, Appion: an integrated, database-driven pipeline to facilitate EM image processing. *Journal of structural biology* **166**, 95 (Apr, 2009).

54. J. A. Mindell, N. Grigorieff, Accurate determination of local defocus and specimen tilt in electron microscopy. *Journal of structural biology* **142**, 334 (Jun, 2003).

55. N. R. Voss, C. K. Yoshioka, M. Radermacher, C. S. Potter, B. Carragher, DoG Picker and TiltPicker: software tools to facilitate particle selection in single particle electron microscopy. *Journal of structural biology* **166**, 205 (May, 2009).

56. C. O. Sorzano *et al.*, A clustering approach to multireference alignment of single-particle projections in electron microscopy. *Journal of structural biology* **171**, 197 (Aug, 2010).

57. A. M. Roseman, FindEM--a fast, efficient program for automatic selection of particles from electron micrographs. *Journal of structural biology* **145**, 91 (Jan-Feb, 2004).

58. Z. Yang, J. Fang, J. Chittuluru, F. J. Asturias, P. A. Penczek, Iterative stable alignment and clustering of 2D transmission electron microscope images. *Structure* **20**, 237 (Feb 8, 2012).

59. S. H. Scheres, R. Nunez-Ramirez, C. O. Sorzano, J. M. Carazo, R. Marabini, Image processing for electron microscopy single-particle analysis using XMIPP. *Nature protocols* **3**, 977 (2008).

60. C. O. Sorzano *et al.*, XMIPP: a new generation of an open-source image processing package for electron microscopy. *Journal of structural biology* **148**, 194 (Nov, 2004).

61. N. Grigorieff, FREALIGN: high-resolution refinement of single particle structures. *Journal of structural biology* **157**, 117 (Jan, 2007).

62. D. Sousa, N. Grigorieff, Ab initio resolution measurement for single particle structures. *Journal of structural biology* **157**, 201 (Jan, 2007).

63. A. Stewart, N. Grigorieff, Noise bias in the refinement of structures derived from single particles. *Ultramicroscopy* **102**, 67 (Dec, 2004).

64. S. H. Scheres, S. Chen, Prevention of overfitting in cryo-EM structure determination. *Nature methods* **9**, 853 (Sep, 2012).

65. P. B. Rosenthal, R. Henderson, Optimal determination of particle orientation, absolute hand, and contrast loss in single-particle electron cryomicroscopy. *J Mol Biol* **333**, 721 (Oct 31, 2003).

66. E. F. Pettersen *et al.*, UCSF Chimera--a visualization system for exploratory research and analysis. *Journal of computational chemistry* **25**, 1605 (Oct, 2004).

67. J. Frank *et al.*, SPIDER and WEB: processing and visualization of images in 3D electron microscopy and related fields. *Journal of structural biology* **116**, 190 (Jan-Feb, 1996).

68. R. Henderson *et al.*, Tilt-pair analysis of images from a range of different specimens in single-particle electron cryomicroscopy. *J Mol Biol* **413**, 1028 (Nov 11, 2011).

69. S. Chen *et al.*, High-resolution noise substitution to measure overfitting and validate resolution in 3D structure determination by single particle electron cryomicroscopy. *Ultramicroscopy* **135C**, 24 (Jun 21, 2013).

70. L. Bordoli, T. Schwede, Automated protein structure modeling with SWISS-MODEL Workspace and the Protein Model Portal. *Methods Mol Biol* **857**, 107 (2012).

71. F. DiMaio, M. D. Tyka, M. L. Baker, W. Chiu, D. Baker, Refinement of protein structures into low-resolution density maps using rosetta. *J Mol Biol* **392**, 181 (Sep 11, 2009).